Supplemental Material: Engineering Weyl phases and nonlinear Hall effects in T_d-$MoTe_2$

Sobhit Singh, Jinwoong Kim, Karin M. Rabe, and David Vanderbilt
Department of Physics and Astronomy, Rutgers University, Piscataway, New Jersey 08854-8019, USA

This Supplemental Material contains information regarding computational details, potential energy profile of the T_0 phase as a function of the cell angle β showing two ferroelastic variants of 1T′ phase, the calculated phonon spectra and elastic constants for T_0, T_d and 1T′ phases. Details related to the Berry curvature dipole moment (BCDM), coordinate of Weyl points, and electronic band structure calculated with and without spin-orbit coupling (SOC) as a function of the polar distortion parameter $\frac{\lambda}{\lambda_0}$, where $\lambda_0 = 0.50$ Å, are also provided. An animation showing the evolution of Weyl points (WPs) as a function of $\frac{\lambda}{\lambda_0}$ is provided as supplemental material in a separate file.

I. COMPUTATIONAL DETAILS

We use Vienna *ab-initio* simulation package (VASP) to perform all the first-principles density-functional theory (DFT) calculations.[1,2] We consider six valence electrons of Mo ($4d^5 5s^1$) and six valence electrons of Te ($5s^2 5p^4$) within the projected-augmented wave (PAW) framework.[3,4] We employ the revised Perdew-Burke-Ernzerhof generalized gradient approximation for solids (PBEsol) to treat exchange and correlation effects.[5] In order to include the on-site Coulomb interaction effects, we use U = 2.8 eV and J = 0.4 eV[6] to simulate Mo $4d$ electrons within the DFT+U scheme (Dudarev approach[7]) at the mean-field level. A plane wave energy cutoff of 600 eV along with a Monkhorst-Pack type k-mesh of size $8 \times 12 \times 4$ are used for electronic convergence. For structural optimization, we use 10^{-4} eV/Å for force convergence, and 10^{-9} eV for energy convergence criteria for electronic self-consistent calculations. Thus optimized cell parameters are $a = 6.329$, $b = 3.450$, $c = 13.485$ Å for the T_d and 1T′ phases. Note that the cell angles for T_d phase are $\alpha = \beta = \gamma = 90°$, whereas the β angle for twin 1T′ phases is 86.4° (I) and 93.6° (II). These values are in good agreement with the previous reports .[6,8–12] The phonon dispersions are computed using the PHONOPY code[13] for a supercell of size $2 \times 2 \times 1$. Two unstable phonon modes, Γ_2^- and Γ_4^+, are observed in the T_0 phase. The phonon modulated structures were fully optimized in all directions except for the direction of the modulation vector. Using Wannier functions based tight-binding Hamiltonians for Mo-$4d$ and Te-$5p$ orbitals, we employ the WANNIER_TOOLS package[14] for analysis of Weyl phase and topological nature of electronic bands. The PyProcar code[15] was used to analyze the electronic band structure.

II. POTENTIAL ENERGY BARRIER PROFILE FOR 1T′- $MoTe_2$ TWIN PHASES

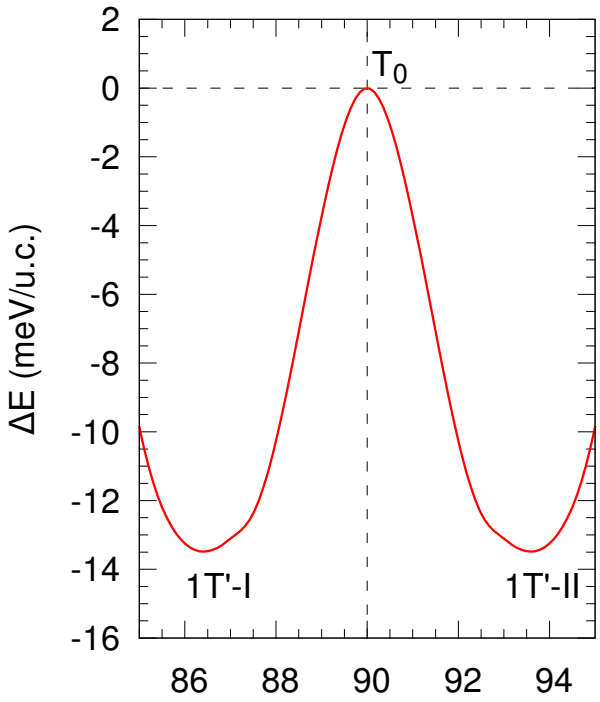

FIG. 1. The double-well potential energy profile of T_0 phase as a function of the cell angle β. The two local minima correspond to two nonpolar ferroelastic phases of 1T′.

The elastic instability (Γ_4^+ mode) causes a shear distortion of the unit cell, making the $\vec{a}$ and $\vec{c}$ lattice vectors nonorthogonal. By modulating the T_0 phase along the Γ_4^+ mode, we obtain a double-well potential energy profile, as shown in Fig. 1, with two local minima at cell angles $\beta = 93.6^\circ$ and $\beta = 87.4^\circ$. These two local minima mark the two ferroelastic twin phases, 1T′-I and 1T′-II, of the monoclinic 1T′ phase. The obtained value of β is in excellent agreement with previous reports.[6,8,16–26] The corresponding interlayer displacement pattern of Mo-Te triple layers in the 1T′-I and 1T′-II phases is: $++++$... and $----$..., respectively. An electron beam induced tunable reversible structural phase transition among these phases has recently been experimentally realized.[27]

III. PHONONS

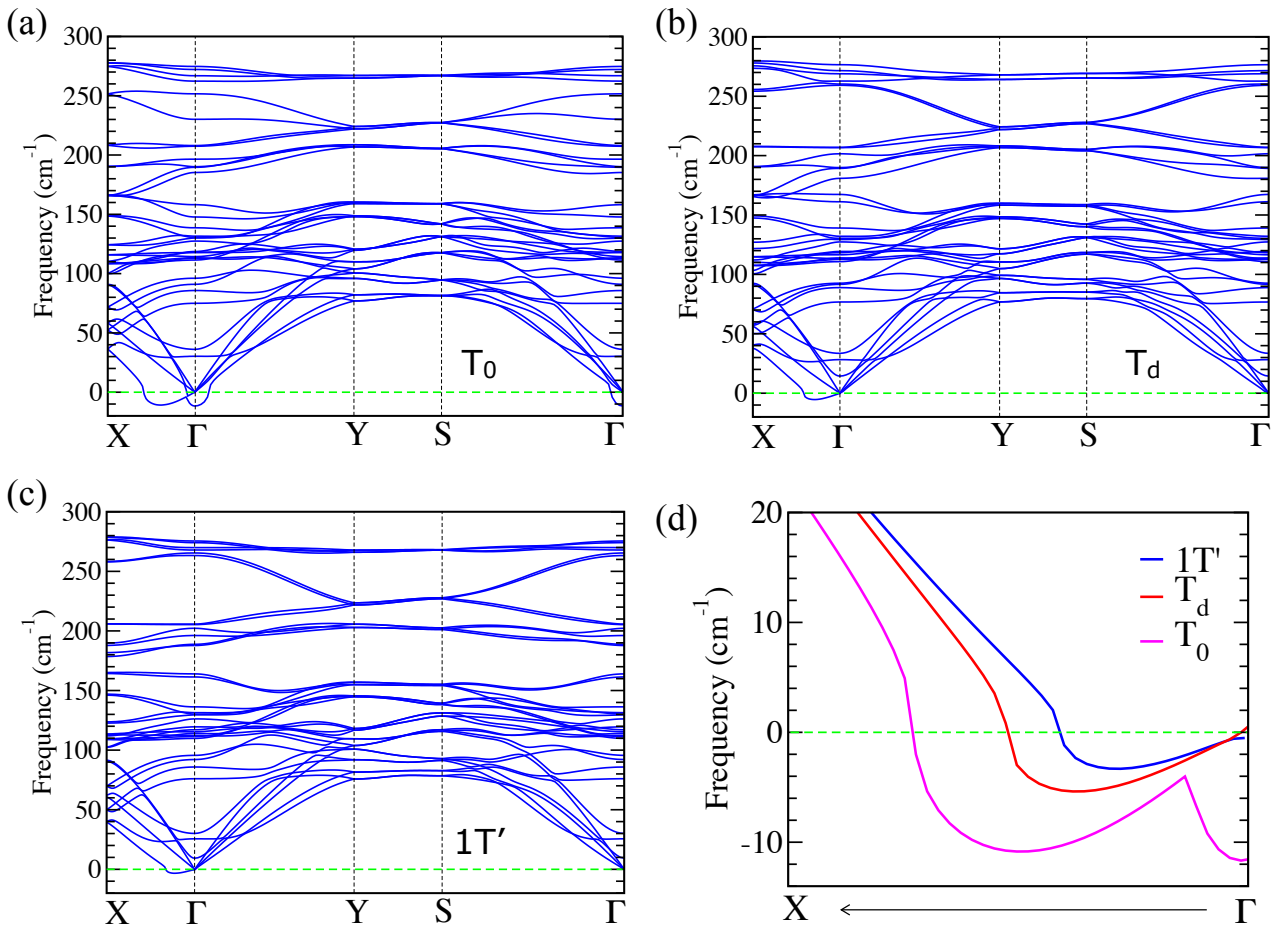

FIG. 2. The phonon spectrum for (a) T_0, (b) T_d, and (c) 1T′ phases calculated using finite-difference approach for a supercell of size $2 \times 2 \times 1$. (d) Comparison of the soft phonon modes in all three phases near the Γ point. Note that the observed elastic instabilities in the T_d and 1T′ phases near Γ point are only due to the poor numerical convergence at $k \to 0$. These, purely numerical, instabilities do not lead to negative elastic constants in the T_d and 1T′ phases. Our elastic constant calculations verify the elastic and mechanical stability of T_d and 1T′ phases, as shown in Table I. However, the unstable phonon mode in the T_0 phase represents a real instability, which yields negative elastic constants and mechanical instability in the structure.

IV. ELASTIC CONSTANTS

TABLE I. This table contains the PBEsol+U calculated elastic constants (C_{ij}, in GPa units) of T_0, T_d, and $1T'$ phases together with the eigen values of C_{ij} matrix and result of the mechanical stability test. The elastic constants were calculated without inclusion of SOC and were converged better than 1 GPa by increasing the size of k-mesh. Inclusion of SOC causes less than 1 GPa difference in the C_{ij} values. The Born-Huang mechanical stability test performed using the MechElastic code[28] proves the elastic instability of the T_0 phase.

Phase	C_{11}, C_{12}, C_{13}, C_{22}, C_{23}, C_{33}, C_{44}, C_{55}, C_{66}	Eigen values of C_{ij} matrix	Mechanical stability test
T_0	−31.8, −50.3, −216.8, 56.2, −152.1, −390.1, 94.1, 47.8, 65.1	$\{-545.7, 41.4, 111.0, 75.6, 94.1, 65.1\}$	Fail
T_d	154.9, 42.0, 21.6, 127.8, 26.0, 23.8, 27.7, 3.9, 51.9	$\{191.9, 98.0, 51.9, 16.6, 4.0, 27.7\}$	Pass
$1T'$	151.0, 36.7, 21.7, 126.4, 28.0, 23.2, 27.1, 2.9, 51.4	$\{184.7, 101.1, 2.8, 14.9, 26.8, 51.7\}$	Pass

V. BERRY CURVATURE DIPOLE MOMENT CALCULATED AT DIFFERENT VALUES OF POLAR DISTORTION PARAMETERS

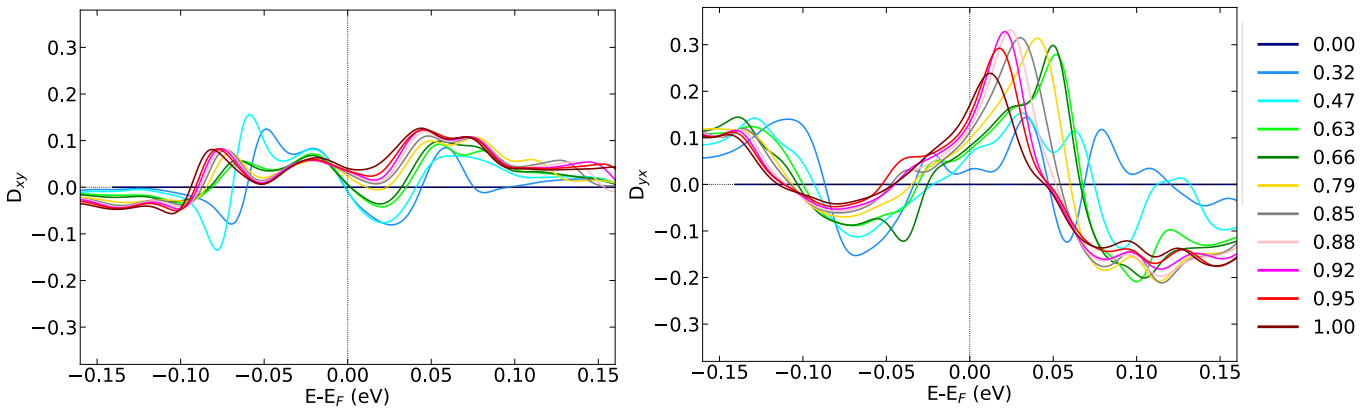

FIG. 3. The non-zero components of Berry curvature dipole moment (BCDM) in bulk $MoTe_2$ computed as a function of the chemical potential for different distorted structures along the polarity reversal path, *i.e.*, for different values of polar distortion parameter $\frac{\lambda}{\lambda_0}$. We use a dense k-mesh of size $278 \times 510 \times 130$ to achieve better convergence of BCDM. Different colors correspond to BCDM data for different values of $\frac{\lambda}{\lambda_0}$. Note that for inversion-symmetric T_0 phase ($\frac{\lambda}{\lambda_0} = 0$), the BCDM is zero. We do not notice any striking enhancement in the BCDM with varying $\frac{\lambda}{\lambda_0}$, except for the slight variations due to the creation/annihilation of new Weyl points with relatively smaller and/or no tilts of Weyl cones and shifting of the Weyl points in the energy-momentum space as we tune $\frac{\lambda}{\lambda_0}$ (see main text for discussion).

VI. BERRY CURVATURE, FERMI-VELOCITY AND THEIR PRODUCT PROJECTED ON THE FERMI-SURFACE

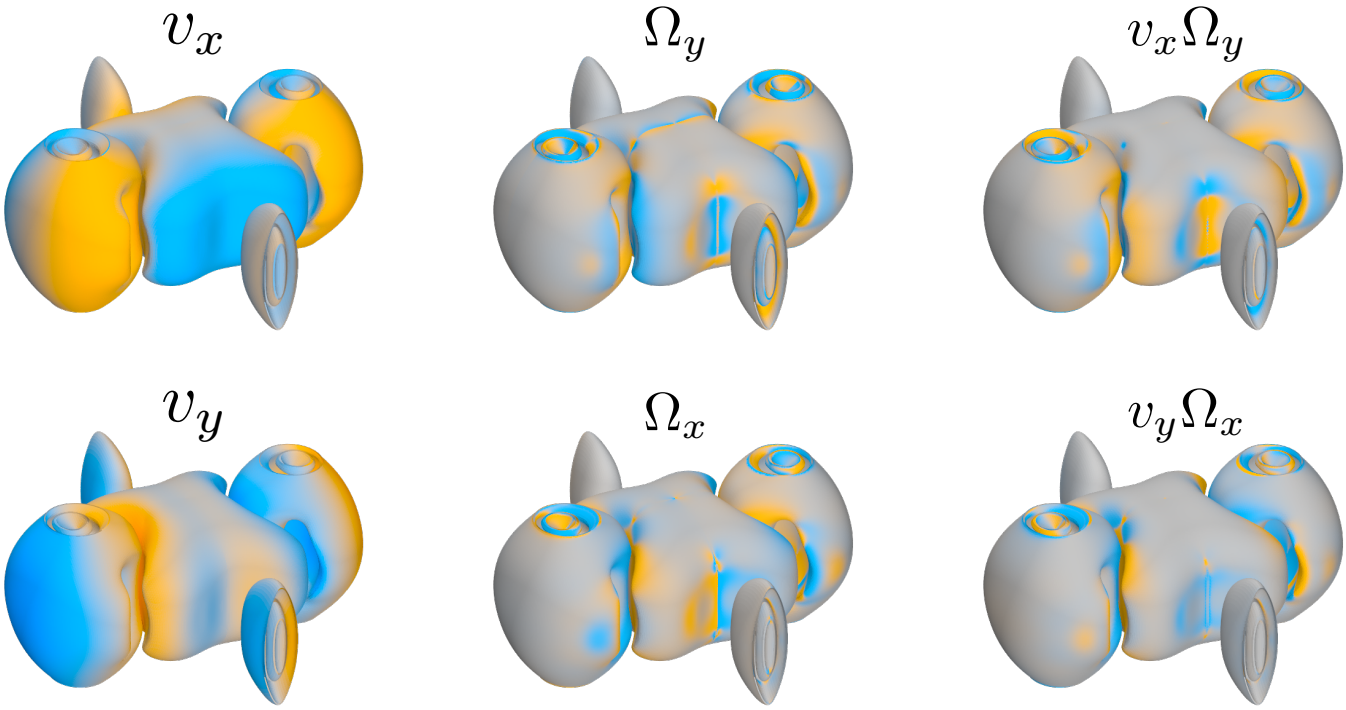

FIG. 4. This figure shows the x and y components of Fermi-velocity (v_x, v_y), Berry curvature (Ω_x, Ω_y), and their product ($v_x\Omega_y$, $v_y\Omega_x$) projected on the Fermi-surface of $MoTe_2$ in T_d-A phase. The $v_x\Omega_y$ and $v_y\Omega_x$ terms relate to the D_{xy} and D_{yx} components of the Berry curvature dipole moment tensor, respectively (see main text for discussion).

VII. COORDINATES OF WEYL POINTS AS A FUNCTION OF POLAR DISTORTION

Table II contains the coordinates of all WPs in the energy and momentum space (units: $k_1\,(\frac{2\pi}{a})$, $k_2\,(\frac{2\pi}{b})$, $k_3\,(\frac{2\pi}{c})$) as a function of the polar distortion parameter $\frac{\lambda}{\lambda_0}$, where $\lambda_0 = 0.50\,$Å. The coordinates are listed only for those $\frac{\lambda}{\lambda_0}$ values at which creation/annihilation of WPs event occurs, *i.e.*, the total number of WPs (N_{WP}) is distinct. An animation showing the evolution of WPs as a function of $\frac{\lambda}{\lambda_0}$ is provided in a separate file.

TABLE II: Coordinates of all WPs calculated at different values of $\frac{\lambda}{\lambda_0}$

$\frac{\lambda}{\lambda_0}$	(k_1, k_2, k_3)	**Chirality**	E-E_F **(meV)**	N_{WP}
0.00	–	–	–	0
0.32	(−0.204, 0.127, −0.225)	−1	39	16
	(0.204, 0.127, 0.225)	1	39	
	(−0.204, −0.127, −0.225)	1	39	
	(0.204, −0.127, 0.225)	−1	39	
	(−0.203, −0.123, 0.229)	1	47	
	(−0.203, 0.123, 0.229)	−1	47	
	(0.203, −0.123, −0.229)	−1	47	
	(0.203, 0.123, −0.229)	1	47	
	(0.190, 0.111, −0.243)	−1	63	
	(−0.190, 0.112, 0.243)	1	63	
	(−0.190, −0.111, 0.243)	−1	63	
	(0.190, −0.112, −0.243)	1	63	
	(0.182, 0.107, 0.248)	−1	64	
	(−0.182, −0.107, −0.248)	−1	64	
	(−0.182, 0.107, −0.248)	1	64	
	(0.182, −0.107, 0.248)	1	64	
0.63	(0.209, 0.158, 0.160)	1	−18	32
	(−0.209, −0.158, −0.160)	1	−18	
	(−0.209, 0.158, −0.160)	−1	−18	
	(0.209, −0.158, 0.160)	−1	−18	
	(0.211, 0.159, −0.154)	1	−19	
	(−0.211, −0.159, 0.154)	1	−19	
	(−0.211, 0.159, 0.154)	−1	−19	
	(−0.211, 0.159, 0.154)	−1	−19	
	(0.096, 0.086, −0.256)	−1	53	
	(−0.096, −0.086, 0.256)	−1	53	
	(0.104, 0.087, 0.257)	−1	54	
	(−0.104, −0.087, −0.257)	−1	54	
	(−0.107, 0.088, −0.256)	1	54	
	(−0.100, 0.087, 0.255)	1	54	
	(0.107, −0.088, 0.256)	1	54	
	(0.100, −0.087, −0.255)	1	54	

TABLE II: Continued on next page

TABLE II: continued from previous page

$\frac{\lambda}{\lambda_0}$	(k_1, k_2, k_3)	**Chirality**	E-E_F **(meV)**	N_{WP}
	(−0.029, −0.071, −0.195)	1	78	
	(0.029, 0.071, 0.195)	1	78	
	(−0.030, −0.071, 0.194)	1	78	
	(0.030, 0.071, −0.194)	1	78	
	(0.029, −0.070, −0.189)	−1	81	
	(−0.029, 0.070, 0.189)	−1	81	
	(−0.027, 0.070, −0.186)	−1	82	
	(0.027, −0.070, 0.186)	−1	82	
	(−0.018, −0.066, 0.129)	−1	102	
	(0.018, 0.066, −0.129)	−1	102	
	(−0.017, 0.066, 0.124)	1	103	
	(0.017, −0.066, −0.124)	1	103	
	(−0.013, −0.066, −0.105)	−1	105	
	(0.013, 0.066, 0.105)	−1	105	
	(−0.013, 0.066, −0.105)	1	105	
	(0.013, 0.066, 0.105)	−1	105	
0.72	(0.210, 0.163, −0.139)	1	−29	28
	(0.208, 0.162, 0.145)	1	−29	
	(−0.208, −0.162, −0.145)	1	−29	
	(−0.210, −0.163, 0.139)	1	−29	
	(−0.210, 0.163, 0.139)	−1	−29	
	(−0.208, 0.162, −0.145)	−1	−29	
	(0.208, −0.162, 0.145)	−1	−29	
	(0.210, −0.163, −0.139)	−1	−29	
	(−0.078, −0.085, 0.250)	−1	41	
	(0.078, 0.085, −0.250)	−1	41	
	(0.087, 0.086, 0.253)	−1	42	
	(−0.087, −0.086, −0.253)	−1	42	
	(−0.091, 0.087, −0.252)	1	43	
	(−0.084, 0.086, 0.250)	1	43	
	(0.091, −0.087, 0.252)	1	43	
	(0.084, −0.086, −0.250)	1	43	
	(−0.040, −0.076, 0.216)	1	55	
	(0.040, 0.076, −0.216)	1	55	
	(0.035, 0.074, 0.212)	1	59	
	(−0.035, −0.074, −0.212)	1	59	
	(−0.037, 0.075, 0.209)	−1	60	
	(0.037, −0.075, −0.209)	−1	60	
	(−0.033, 0.073, −0.206)	−1	63	
	(0.033, −0.073, 0.206)	−1	63	
	(0.012, −0.066, −0.068)	1	106	
	(0.012, −0.066, −0.068)	1	106	

TABLE II: Continued on next page

TABLE II: continued from previous page

$\frac{\lambda}{\lambda_0}$	(k_1, k_2, k_3)	**Chirality**	E-E_F **(meV)**	N_{WP}
	(−0.012, −0.066, 0.073)	−1	106	
	(0.012, 0.066, −0.073)	−1	106	
0.79	(0.209, 0.165, −0.129)	1	−41	24
	(−0.209, 0.165, 0.129)	−1	−41	
	(−0.209, −0.165, 0.129)	1	−41	
	(0.209, −0.165, −0.129)	−1	−41	
	(0.207, 0.165, 0.136)	1	−40	
	(−0.207, −0.165, −0.136)	1	−40	
	(−0.207, 0.165, −0.136)	−1	−40	
	(0.207, −0.165, 0.136)	−1	−40	
	(0.077, 0.085, 0.250)	−1	29	
	(−0.077, −0.085, −0.250)	−1	29	
	(−0.071, 0.084, 0.244)	1	29	
	(0.071, −0.084, −0.244)	1	29	
	(−0.082, 0.086, −0.249)	1	30	
	(0.082, −0.086, 0.249)	1	30	
	(−0.044, 0.078, 0.220)	−1	40	
	(0.044, −0.078, −0.220)	−1	40	
	(0.039, 0.077, 0.218)	1	42	
	(−0.039, −0.077, −0.218)	1	42	
	(−0.036, 0.076, −0.212)	−1	47	
	(0.036, −0.076, 0.212)	−1	47	
	(−0.011, 0.066, 0.030)	1	99	
	(0.011, −0.066, −0.030)	1	99	
	(−0.010, −0.066, 0.024)	−1	100	
	(0.010, 0.066, −0.024)	−1	100	
0.85	(0.208, 0.167, −0.121)	1	−40	20
	(0.206, 0.166, 0.128)	1	−40	
	(−0.206, −0.166, −0.128)	1	−40	
	(−0.208, 0.167, 0.121)	−1	−40	
	(−0.208, −0.167, 0.121)	1	−40	
	(0.208, −0.167, −0.121)	−1	−40	
	(−0.206, 0.166, −0.128)	−1	−39	
	(0.206, −0.166, 0.128)	−1	−39	
	(−0.066, −0.085, −0.244)	−1	26	
	(0.066, 0.085, 0.244)	−1	26	
	(−0.073, 0.086, −0.245)	1	27	
	(0.073, −0.086, 0.245)	1	27	
	(−0.044, −0.080, −0.225)	1	34	
	(0.044, 0.080, 0.225)	1	34	
	(0.040, −0.078, 0.217)	−1	40	
	(−0.040, 0.078, −0.217)	−1	40	

TABLE II: Continued on next page

TABLE II: continued from previous page

$\frac{\lambda}{\lambda_0}$	(k_1, k_2, k_3)	**Chirality**	E-E_F **(meV)**	N_{WP}
	(−0.014, 0.066, 0.013)	1	103	
	(0.014, −0.066, −0.013)	1	103	
	(−0.014, −0.066, 0.009)	−1	103	
	(0.014, 0.066, −0.009)	−1	103	
0.92	(0.207, 0.169, −0.113)	1	−44	16
	(−0.207, −0.169, 0.113)	1	−44	
	(0.205, 0.168, 0.122)	1	−44	
	(0.206, −0.169, −0.113)	−1	−44	
	(−0.206, 0.169, 0.113)	−1	−44	
	(−0.205, −0.168, −0.122)	1	−44	
	(−0.205, 0.168, −0.122)	−1	−44	
	(0.205, −0.168, 0.122)	−1	−44	
	(0.063, −0.085, 0.239)	1	20	
	(−0.063, 0.085, −0.239)	1	20	
	(−0.045, 0.081, −0.223)	−1	27	
	(0.045, −0.081, 0.223)	−1	27	
	(−0.017, 0.067, 0.000)	1	101	
	(0.017, −0.067, −0.000)	1	101	
	(−0.017, −0.067, 0.000)	−1	101	
	(0.017, 0.067, −0.000)	−1	101	
1.00	(0.205, −0.170, −0.105)	−1	−38	12
	(0.205, 0.170, −0.105)	1	−38	
	(−0.205, −0.170, 0.105)	1	−38	
	(−0.205, 0.170, 0.105)	−1	−38	
	(0.203, 0.170, 0.114)	1	−38	
	(−0.203, 0.170, −0.114)	−1	−38	
	(−0.203, −0.170, −0.114)	1	−38	
	(0.203, −0.170, 0.114)	−1	−38	
	(−0.020, −0.068, 0.000)	−1	108	
	(−0.021, 0.068, 0.000)	1	108	
	(0.021, −0.068, 0.000)	1	108	
	(0.020, 0.068, 0.000)	−1	108	

TABLE II: This table ends here.

VIII. TOPOLOGICAL CLASSIFICATION OF T_0 AND 1T′ PHASES

Using vasp2trace code,[29] we check the topological behavior of the nonpolar T_0 and 1T′ phases. We find that both nonpolar phases have z_4=2, and both belong to a strong topological class 20 as defined in Ref. [29]. This finding verifies the presence of a second-order topological insulating phase in T_0 and 1T′ $MoTe_2$. Due to the presence of gapless Weyl points, the T_d phase cannot exhibit a higher-order (> 1) topological character although it satisfies all the other conditions to be a second-order topological insulator.[29,30] When all Weyl points annihilate each other and a direct bandgap opens in the T_0 phase, the system enters into a second-order topological phase.

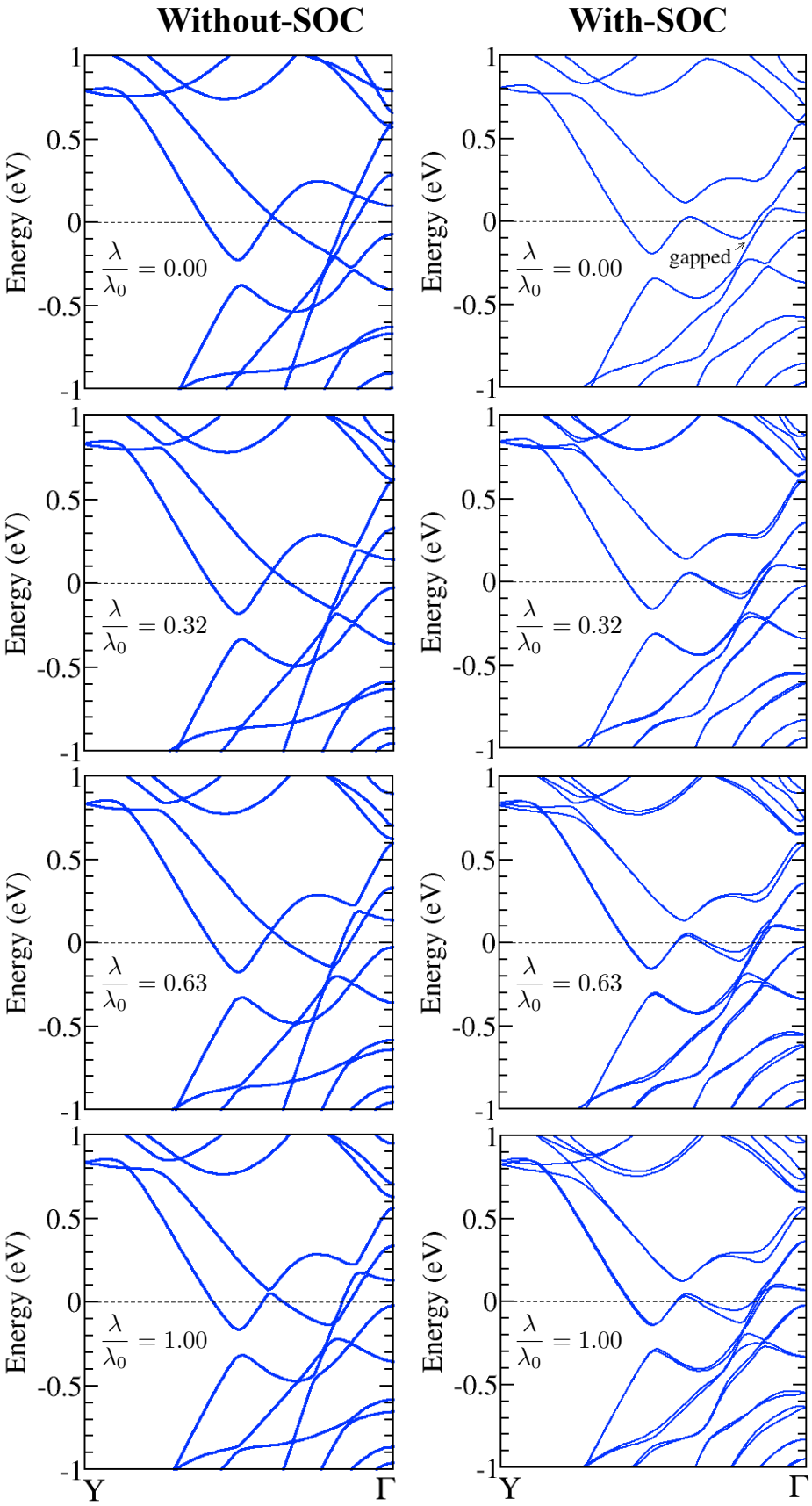

FIG. 5. The electronic band structure calculated along the Γ-Y direction of Brillouin zone for different values of λ/λ_0 parameters, and with- (right panel) and without- (left panel) inclusion of SOC. Note the band gap (SOC) at $\lambda/\lambda_0 = 0.00$, *i.e.*, for the T_0 phase.

IX. DISPERSION OF BANDS NEAR WEYL POINTS IN THE T_d PHASE

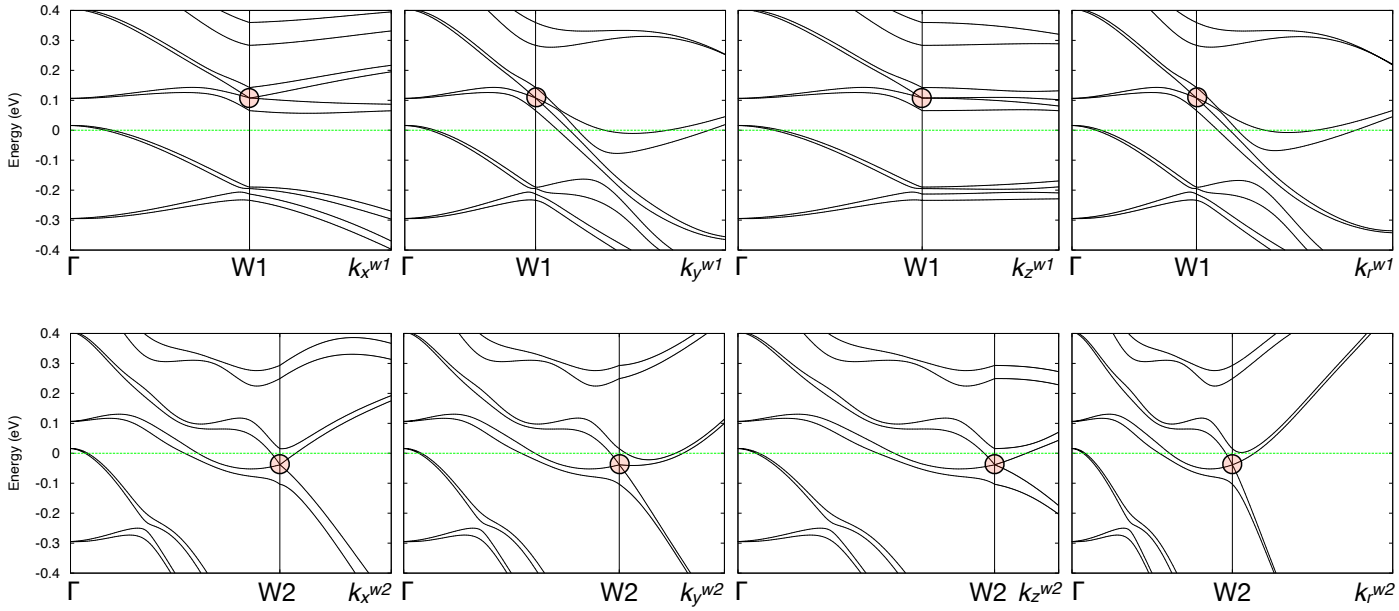

FIG. 6. The electronic band structure calculated in the vicinity of WPs (with SOC) along different directions in the momentum space of T_d-$MoTe_2$. Shaded circles mark the position of a WP. Dotted horizontal line represents the Fermi energy. Top panel shows the band dispersions near a type-II W1 Weyl node located above the Fermi level. The direct coordinates of the W1, k_x^{W1}, k_y^{W1}, k_z^{W1}, and k_r^{W1} points are (0.020, 0.068, 0.000), (0.120, 0.068, 0.000), (0.020, 0.168, 0.000), (0.020, 0.068, 0.200), and (0.040, 0.176, 0.000), respectively. Bottom panel shows the band dispersions near a type-II W2 Weyl node located below the Fermi level. The direct coordinates of the W2, k_x^{W2}, k_y^{W2}, k_z^{W2}, and k_r^{W2} points are (0.203, 0.170, 0.114), (0.403, 0.170, 0.114), (0.203, 0.370, 0.114), (0.203, 0.170, 0.314), and (0.406, 0.340, 0.228), respectively. The type-II nature of W2 WP can be noticed along Γ–k_y direction.

X. DISTRIBUTION OF ALL WEYL POINTS IN THE BRILLOUIN ZONE

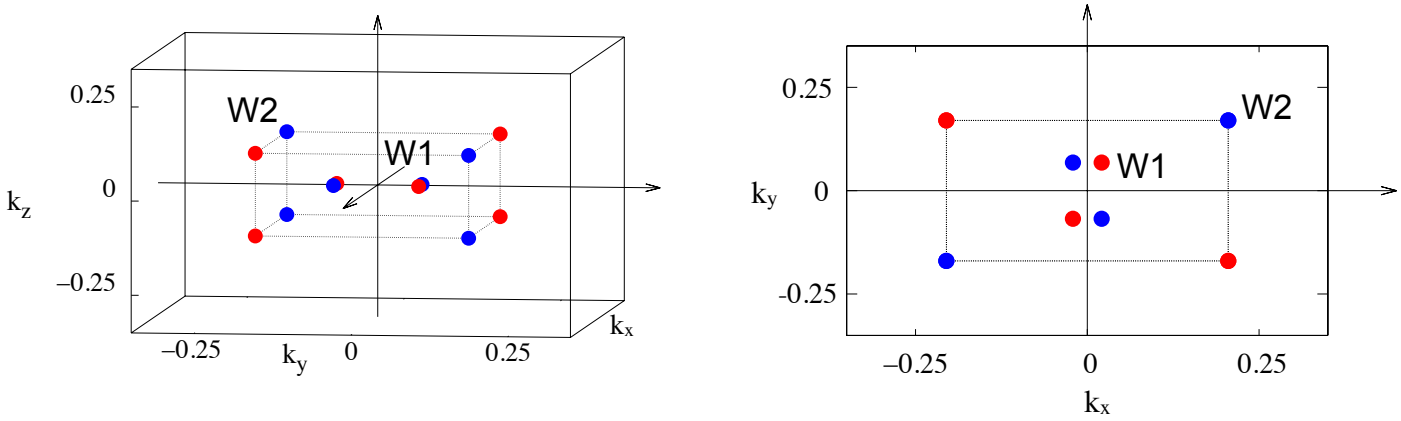

FIG. 7. Distribution of all Weyl points in the Brillouin zone for the T_d-A phase, shown from the top and the side views. Red/blue dots depict +/− chiralities of the WPs. Chiralities of all WPs switches in the T_d-B phase.

[1] G. Kresse and J. Furthmüller, Phys. Rev. B **54**, 11169 (1996).
[2] G. Kresse and J. Furthmüller, Computational Materials Science **6**, 15 (1996).
[3] P. E. Blöchl, Phys. Rev. B **50**, 17953 (1994).
[4] G. Kresse and D. Joubert, Phys. Rev. B **59**, 1758 (1999).
[5] J. P. Perdew, A. Ruzsinszky, G. I. Csonka, O. A. Vydrov, G. E. Scuseria, L. A. Constantin, X. Zhou, and K. Burke, Phys. Rev. Lett. **100**, 136406 (2008).
[6] N. Xu, Z. W. Wang, A. Magrez, P. Bugnon, H. Berger, C. E. Matt, V. N. Strocov, N. C. Plumb, M. Radovic, E. Pomjakushina, K. Conder, J. H. Dil, J. Mesot, R. Yu, H. Ding, and M. Shi, Phys. Rev. Lett. **121**, 136401 (2018).
[7] S. L. Dudarev, G. A. Botton, S. Y. Savrasov, C. J. Humphreys, and A. P. Sutton, Phys. Rev. B **57**, 1505 (1998).
[8] R. Clarke, E. Marseglia, and H. P. Hughes, Philosophical Magazine B **38**, 121 (1978).
[9] S.-Y. Chen, T. Goldstein, D. Venkataraman, A. Ramasubramaniam, and J. Yan, *Nano Letters*, Nano Letters **16**, 5852 (2016).
[10] X.-J. Yan, Y.-Y. Lv, L. Li, X. Li, S.-H. Yao, Y.-B. Chen, X.-P. Liu, H. Lu, M.-H. Lu, and Y.-F. Chen, npj Quantum Materials **2**, 31 (2017).
[11] A. N. Berger, E. Andrade, A. Kerelsky, D. Edelberg, J. Li, Z. Wang, L. Zhang, J. Kim, N. Zaki, J. Avila, C. Chen, M. C. Asensio, S.-W. Cheong, B. A. Bernevig, and A. N. Pasupathy, npj Quantum Materials **3**, 2 (2018).
[12] N. Aryal and E. Manousakis, Phys. Rev. B **99**, 035123 (2019).
[13] A. Togo and I. Tanaka, Scr. Mater. **108**, 1 (2015).
[14] Q. Wu, S. Zhang, H.-F. Song, M. Troyer, and A. A. Soluyanov, Computer Physics Communications **224**, 405 (2018).
[15] U. Herath, P. Tavadze, X. He, E. Bousquet, S. Singh, F. Muoz, and A. H. Romero, Computer Physics Communications , 107080 (2019).
[16] Y. Sun, S.-C. Wu, M. N. Ali, C. Felser, and B. Yan, Phys. Rev. B **92**, 161107 (2015).
[17] A. A. Soluyanov, D. Gresch, Z. Wang, Q. Wu, M. Troyer, X. Dai, and B. A. Bernevig, Nature **527**, 495 (2015).
[18] Y. Qi, P. G. Naumov, M. N. Ali, C. R. Rajamathi, W. Schnelle, O. Barkalov, M. Hanfland, S.-C. Wu, C. Shekhar, Y. Sun, V. Süß, M. Schmidt, U. Schwarz, E. Pippel, P. Werner, R. Hillebrand, T. Förster, E. Kampert, S. Parkin, R. J. Cava, C. Felser, B. Yan, and S. A. Medvedev, Nature Communications **7**, 11038 (2016).
[19] L. Huang, T. M. McCormick, M. Ochi, Z. Zhao, M.-T. Suzuki, R. Arita, Y. Wu, D. Mou, H. Cao, J. Yan, N. Trivedi, and A. Kaminski, Nature Materials **15**, 1155 (2016).
[20] Z. Wang, D. Gresch, A. A. Soluyanov, W. Xie, S. Kushwaha, X. Dai, M. Troyer, R. J. Cava, and B. A. Bernevig, Phys. Rev. Lett. **117**, 056805 (2016).
[21] A. Tamai, Q. S. Wu, I. Cucchi, F. Y. Bruno, S. Riccò, T. K. Kim, M. Hoesch, C. Barreteau, E. Giannini, C. Besnard, A. A. Soluyanov, and F. Baumberger, Phys. Rev. X **6**, 031021 (2016).
[22] H.-J. Kim, S.-H. Kang, I. Hamada, and Y.-W. Son, Phys. Rev. B **95**, 180101 (2017).
[23] D. Rhodes, R. Schönemann, N. Aryal, Q. Zhou, Q. R. Zhang, E. Kampert, Y.-C. Chiu, Y. Lai, Y. Shimura, G. T. McCandless, J. Y. Chan, D. W. Paley, J. Lee, A. D. Finke, J. P. C. Ruff, S. Das, E. Manousakis, and L. Balicas, Phys. Rev. B **96**, 165134 (2017).
[24] A. Crepaldi, G. Autès, G. Gatti, S. Roth, A. Sterzi, G. Manzoni, M. Zacchigna, C. Cacho, R. T. Chapman, E. Springate, E. A. Seddon, P. Bugnon, A. Magrez, H. Berger, I. Vobornik, M. Kalläne, A. Quer, K. Rossnagel, F. Parmigiani, O. V. Yazyev, and M. Grioni, Phys. Rev. B **96**, 241408 (2017).
[25] H. Takahashi, T. Akiba, K. Imura, T. Shiino, K. Deguchi, N. K. Sato, H. Sakai, M. S. Bahramy, and S. Ishiwata, Phys. Rev. B **95**, 100501 (2017).
[26] C. Heikes, I.-L. Liu, T. Metz, C. Eckberg, P. Neves, Y. Wu, L. Hung, P. Piccoli, H. Cao, J. Leao, J. Paglione, T. Yildirim, N. P. Butch, and W. Ratcliff, Phys. Rev. Materials **2**, 074202 (2018).
[27] F.-T. Huang, S. Joon Lim, S. Singh, J. Kim, L. Zhang, J.-W. Kim, M.-W. Chu, K. M. Rabe, D. Vanderbilt, and S.-W. Cheong, Nature Communications **10**, 4211 (2019).
[28] S. Singh, I. Valencia-Jaime, O. Pavlic, and A. H. Romero, Phys. Rev. B **97**, 054108 (2018).
[29] M. G. Vergniory, L. Elcoro, C. Felser, N. Regnault, B. A. Bernevig, and Z. Wang, Nature **566**, 480 (2019).
[30] Z. Wang, B. J. Wieder, J. Li, B. Yan, and B. A. Bernevig, Phys. Rev. Lett. **123**, 186401 (2019).